



HAL
open science

Low-Cost Tin Compounds as Seeds for the Growth of Silicon Nanowire–Graphite Composites Used in High-Performance Lithium-Ion Battery Anodes

Caroline Keller, Saravanan Karuppiah, Martin Raaen, Jingxian Wang, Patrice Perrenot, Dmitry Aldakov, Peter Reiss, Cédric Haon, Pascale Chenevier

► **To cite this version:**

Caroline Keller, Saravanan Karuppiah, Martin Raaen, Jingxian Wang, Patrice Perrenot, et al.. Low-Cost Tin Compounds as Seeds for the Growth of Silicon Nanowire–Graphite Composites Used in High-Performance Lithium-Ion Battery Anodes. *ACS Applied Energy Materials*, 2023, 6 (10), pp.5249-5258. 10.1021/acsaem.3c00178 . hal-04089081

HAL Id: hal-04089081

<https://hal.science/hal-04089081>

Submitted on 16 Nov 2023

HAL is a multi-disciplinary open access archive for the deposit and dissemination of scientific research documents, whether they are published or not. The documents may come from teaching and research institutions in France or abroad, or from public or private research centers.

L'archive ouverte pluridisciplinaire **HAL**, est destinée au dépôt et à la diffusion de documents scientifiques de niveau recherche, publiés ou non, émanant des établissements d'enseignement et de recherche français ou étrangers, des laboratoires publics ou privés.

Low-cost tin compounds as seeds for the growth of silicon nanowires-graphite composites used in high-performance lithium-ion battery anodes

Caroline Keller^{†,‡}, Saravanan Karupiah^{†,‡}, Martin Raaen[†], Jingxian Wang^{†,‡,‡}, Patrice Perrenot[§], Dmitry Aldakov[†], Peter Reiss[†], Cédric Haon^{‡} and Pascale Chenevier^{*†}*

[†]Univ. Grenoble Alpes, CEA, CNRS, IRIG, SYMMES, STEP, 38000 Grenoble, France

[‡]Univ. Grenoble Alpes, CEA, LITEN, DEHT, 38000 Grenoble, France

[‡]Univ. Grenoble Alpes, CEA, CNRS, IRIG, LCBM, SolHyCat, 38000 Grenoble, France

[§] Univ. Grenoble Alpes, CEA, LITEN, DTNM, 38000 Grenoble, France

KEYWORDS. tin seeds, silicon-graphite, lithium ion batteries, low-cost anode, high loading

ABSTRACT. Nanostructured silicon-graphite composites range among the best options for achieving next generation high-energy anodes for high performance lithium-ion batteries. Growing silicon nanowires on graphite gives access to composites with high capacity and stability, as the silicon distributes homogeneously in the electrode, and the direct contact provides enhanced mechanical stability even in silicon-rich (~~>30 wt%~~) active materials. However, cost effective production of such composites remains a challenge. Here we introduce low-cost catalysts, tin

sulfide and tin oxide, enabling silicon nanowire growth at lower temperature than with widely used gold catalysts, and investigate their impact on the composite nanostructure and composition. The small difference detected in the composition of the products obtained with both catalysts required the development of a reliable method to measure the low-level oxygen content and distribution within the composite. It revealed that oxygen from the SnO₂ growth seeds is incorporated into the silicon nanowires, while no sulfur from the SnS catalyst could be detected. We show that SnS seeds results in a Si-rich anode material (22wt% Si) of superior initial Coulombic efficiency of 81%, while capacity, stability in cycling and rate capability are less affected by the choice of the catalyst. The composite anodes, optimized for a capacity of 1000 mAh g⁻¹ at C/5 rate, deliver an areal capacity up to 3.6 mAh cm⁻² and 82% capacity retention over 200 cycles. Their rate capability of 780 mAh g⁻¹ at 5C surpasses that of gold-seeded silicon-graphite composites. The insight obtained from this study provides guidance for the reliable low-cost synthesis and quality control of silicon-containing active materials for Li-ion battery anodes.

Increasing the capacity of the anode active material in lithium-ion batteries (LIBs) is an efficient way to enhance their energy density, and thus reduce their weight. The optimal specific capacity for the anode is around 1000 mAh/g,¹ taking into account the limited capacity of the present cathode active materials. Thanks to the high theoretical capacity of 3579 mAh g⁻¹ of silicon and the compatible redox potentials of Si (0.4V vs Li⁺/Li) and graphite (0.1 V), silicon-graphite (SiGt) composites offer a wide range of possibilities towards this target. We recently demonstrated that our indigenously developed composites of silicon nanowires (SiNWs) directly grown one-pot on graphite perform well in long-term cycling due to the improved mechanical integrity of the

electrode *via* an effective nanoarchitecture engineering.² However, SiNW growth requires metal seeds, for which gold is the standard and most active catalyst.³

Gold as a seed metal increases of course the cost of the SiGt composite, and previous literature reported a significant capacity fade in cycling due to the gold seeds.⁴ A wide series of alternative metals can be used as SiNW seeds, such as copper (Cu),⁵ nickel (Ni)⁶ or tin (Sn).⁷ Sn appears as a particularly attractive candidate for several reasons. First, the Sn-Si eutectic temperature at 232°C allows for SiNW growth at lower temperature (Au-Si eutectic at 363°C). Second, Sn is also a lithium-alloying material that will add to the active material's capacity. Nevertheless, Sn(0) oxidizes readily in air,^{8,9} and tin must be in its reduced state to form a Sn-Si eutectic for SiNW growth. Early studies used *in-situ* generated Sn seed particles from the dewetting of Sn-metal films deposited on a substrate prior to SiNW growth.^{7,10} For bulk growth of SiNWs in a superfluidic solvent,⁸ Sn nanoparticles were synthesized *in-situ* from a molecular Sn source in parallel with the growth.

Here, we use nanoparticles of simple Sn-based compounds in colloidal suspension for an efficient impregnation of the graphite powder with the seed catalyst. We investigate two compounds: tin sulfide and tin dioxide. SnS nanoparticles, obtained with a narrow control of diameter by colloidal synthesis,¹¹ provide an air-stable source of Sn with a low content in oxygen. Alternatively, a number of literature studies reported that SnO₂ could be used as a SiNW seed.^{10,12-14} We thus compare SnS seeds with SnO₂ particles as a low cost source of Sn, with a wide distribution of sizes and higher oxidation degree. From SnS and SnO₂ seeds, we obtain two SiGt composites named SnS-SiGt and SnO₂-SiGt. We compare in detail their structure and composition, in particular their oxygen content as oxygen present in the active material will increase lithium consumption in the solid-electrolyte interphase (SEI). Interestingly, the electrochemical

performances of SnS-SiGt and SnO₂-SiGt in terms of capacity, cycling stability and rate capability were increased as compared to Au seeded SiGt composites. Our approach sheds light on the engineering of SiGt composite anodes for lithium-ion batteries (LIB) with a desirable morphology and composition, to stabilize high-energy anodes. This method is ~~suitable for~~ easily scalable and could be translated to industrial mass production in advanced LIBs ~~due to its easy scalability~~.

RESULTS AND DISCUSSION

SiGt composite growth

Seed size tuning is a potent method to control the diameter of SiNWs, which later directs the electrochemical performance of SiNW-containing anodes in LIB.¹⁵ As SnS seeds for the growth of SiNWs, we thus chose nanocrystals (NCs) with a narrow size distribution around 6 nm (Figure S1a), synthesized by colloidal growth. SnS NCs are stabilized by a combination of surface ligands (trioctylphosphine, oleate and oleylamine). SnO₂ nanoparticles (NPs), purchased as an aqueous suspension, show a wide size distribution from 10 to 100 nm (Figure S1b).

We first optimized the growth conditions at a lower temperature than for SiNWs from gold seeds. Diphenylsilane is a very favorable silicon source for SiNW growth from gold catalysts¹⁵⁻¹⁷ at 420-500°C but tin catalysts are active at much lower temperature of 250-400 °C,^{18,19} at which diphenylsilane reactivity is more sluggish. We thus substituted with a mixture of diphenylsilane and phenylsilane (70/30 mol%) as the silicon precursor, to increase the reactivity at 380 °C (reaction time: 4 hours).²⁰ Si loadings up to 25 wt% were attained, with a Sn content of about Sn/Si = 15 wt%.

Note that no preliminary Sn reduction was performed before SiNW growth,²⁰ although in the literature a preliminary step of reduction by hydrogen was found necessary.^{10,12,13} SnO₂ NPs are

stable up to at least 1000 °C,²¹ and SnS NCs up to 350 °C.²² However, the highly reducing conditions of the growth in our high pressure reactor are expected to reduce Sn(IV) and Sn(II) compounds to Sn(0) *in-situ*, since the pressure of the phenylsilane/diphenylsilane hydride²³ vapors attains 1 bar at 250 °C.²⁰

No significant difference between SnS and SnO₂ seeds was observed in pressure/temperature records at the beginning of growth, the pressure starting to rise by 170 ± 20 °C (Figure S2). However, SnS NCs were more active as a catalyst than SnO₂ NPs, yielding about 40% more growth for the same amount of catalyst. The lower activity of SnO₂ NPs was compensated for by increasing the quantity of seeds (160 mg of SnO₂ NPs instead of 100 mg of SnS NCs).

SnS-SiGt and SnO₂-SiGt composites show a similar structure on SEM and TEM micrographs (Figure 1). The obtained SiNWs have an average diameter of about 35 nm with a wide size distribution from 8 to 100 nm. It is noteworthy that the SiNW diameter is not directly correlated to the seed size. Indeed the rate of growth of a SiNW depends on the curvature of the eutectic droplet and its supersaturation with Si³, so that an optimal diameter is thermodynamically favored for a given set of growth conditions. As shown by high partial pressure of silane favors small SiNWs, and a low silane pressure favors large diameters so that small seeds have time to merge before growth starts. Small amounts of SiNWs of 11 nm could easily be obtained from SnS seeds when the growth was performed in a sealed glass tube, the fast heating of which allows for a fast rise in silane pressure (Figure S3). Alternatively, we have shown in our recent study using SnO₂ catalyst nanoparticles in the presence of Ar gas that a kinetic control of the SiNW diameter is possible²⁰: increasing the overall pressure shifts up the onset of the reaction by 100 °C, and reduces the SiNW diameter to 12 nm with a narrow size distribution.

The SiNWs obtained in the present work show a crystalline core according to TEM (Figure 1c,f), electron (Figure S4e) and X-ray diffraction (Figure S6) and a kinked structure already reported for Sn-based SiNW growth.^{7,8} In the purpose of making LIB anode materials, intermediate diameters (20-40 nm) are most appropriate.¹⁵ It is a trade-off between larger diameters, which reduce the specific area and thus the amount of SEI to be formed during the first cycle, and smaller diameters, which reduce the capacity loss due to the formation of $c\text{-Li}_{15}\text{Si}_4$ at the end of lithiation.

The specific areas of SnS-SiGt and SnO₂-SiGt, measured by the BET method, were the same at $32 \pm 3 \text{ m}^2/\text{g}$. This value is in line with the expected specific area calculated from the composition obtained via quantitative elemental analysis by EDX (Table 1) and the specific areas of pure graphite ($6 \text{ m}^2/\text{g}$) and pure SiNWs with the same average diameter¹⁵ ($92 \text{ m}^2/\text{g}$).

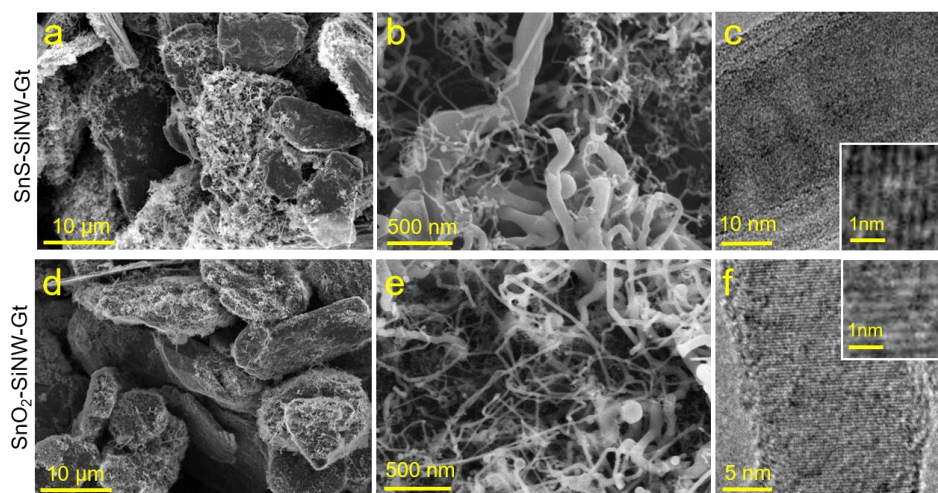


Figure 1. Electronic microscopy images of SnS-SiGt (a,b,c) and SnO₂-SiGt (d,e,f) by SEM (a,b,d,e) and TEM (c,f). Back scattered electron images are displayed in Figure S4 and S5.

Oxygen content and localization in the SiGt composites

An important difference between the SnS and SnO₂ catalysts is the quantity of oxygen brought in the growth vessel. SnO₂ reduction produces water, which reacts with silanes and with crystalline silicon to form silanol bonds Si-OH.²⁴ This reaction, slow at room temperature, is a fast process above 250°C.²⁵ As oxygen has a detrimental effect on the anode capacity retention, we measured carefully the O content in composites by XPS and quantitative EDX. Table 1 reports the average elemental compositions in SnS-SiGt and SnO₂-SiGt composites, measured by EDX. As expected, oxygen is twice more present in the sample when SnO₂ is used as the catalyst. The carbon, tin and silicon contents are in good agreement with the estimates by weighing the reagents and products.

Table 1. Composition in weight of SnS-SiGt and SnO₂-SiGt measured by quantitative EDX. The composition of pure graphite and pure SiNWs grown on NaCl from SnS and SnO₂ catalysts are given as references. ^(a) The detection limit of EDX is around 0.1%

wt% by EDX	C	Sn	Si	O	S
SnS-SiGt	76 ± 5	3.6 ± 0.9	19 ± 4	1.3 ± 0.2	≈ 0.02 ^a
SnO₂-SiGt	70 ± 2	5.2 ± 0.7	22 ± 1	2.3 ± 0.2	< 0.01
Gt	97.5 ± 0.1	-	-	2.05 ± 0.04	< 0.01
SnS-SiNW	0.7 ± 0.1	21 ± 2	77 ± 2	1.6 ± 0.2	0.1 ± 0.05 ^a
SnO ₂ -SiNW	1.0 ± 0.1	23.5 ± 0.5	73 ± 1	2.3 ± 0.1	< 0.01

Tableau mis en forme

SiGt composites are composed of several phases (SiNW, graphite (Gt), and tin nanoparticles SnNP) which can all contain oxygen, with different impact on the anode material cycling performance. Oxygen in silicon or tin consumes lithium by forming Li₂O at the first lithiation, and then will form water and ultimately HF by reaction with the electrolyte,²⁶ while oxygen covalently

linked to graphite will not. Besides, SiNW also contain C from their native organic layer of phenyls.¹⁶ To sort out the contributions of each component, we computed the O content in Si and Sn through an in-depth elemental analysis. The composites were pressed into dense pellets for quantitative EDX analysis on a calibrated SEM. A series of measurements was performed on each pellet from small regions ($20 \times 20 \mu\text{m}^2$) close to the graphite particle size, so that different SiNW/Gt ratios were probed. Correlations between elemental ratios allowed inferring the relative O content in the different phases of the composite. Figure 2 presents the correlation diagrams of Sn with Si, and of O with Si, taking C as the reference. This analysis was carried out on 3 independent samples of each kind with consistent results.

Figure 2a shows that Sn and Si contents are proportional in both composites, indicating that the ratio of Si and Sn is homogeneous all over the material. This indicates a homogeneous average SiNW length in the composite, and thus a homogeneous growth process and growth rate in the graphite powder. However, as Si and Sn are everywhere present in the same ratio, it will not be possible to distinguish whether trace elements belong to the silicon or the tin phases by such correlations. We will thus consider the ensemble SiNW-SnNP as one phase.

We now try to localize O as a trace element in relation to the SiNW-SnNP phase, by looking at the correlation of O and Si contents in Figure 2b. A sharp discrepancy appears between the two composites. For SnS-SiGt, the O content is independent of the Si content. As the O/C weight ratio is constant, it shows that all O is located in the graphite phase. As for SnO_2 -SiGt, the O content increases linearly with the Si content, showing that a significant part of the O is located in the SiNW-SnNP phase. Other correlations, drawn between O and Sn for instance, give similar results (Figure S7).

Table 2. Calculated O content in the components of the composites, from EDX correlation

O content (wt%)	in graphite	in SiNW-SnNP
Pristine Gt	2.05 ± 0.04	-
SnS-SiGt	1.8 ± 0.15	0.0 ± 0.3
SnO ₂ -SiGt	1.6 ± 0.15	5 ± 1

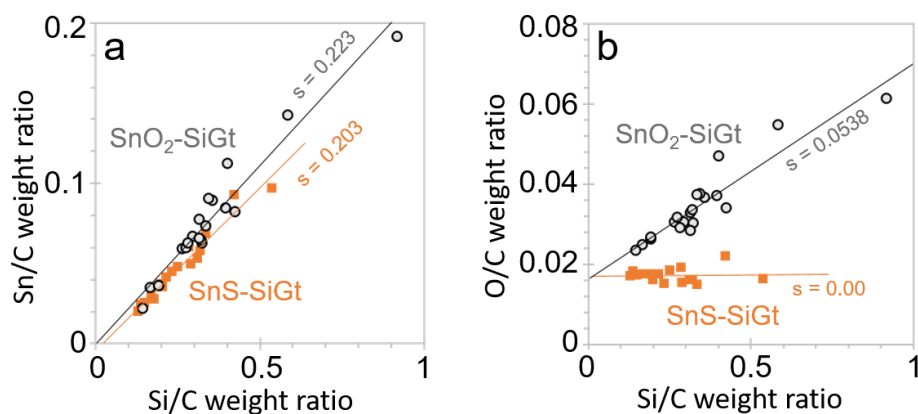


Figure 2. Correlation diagrams for elemental analysis by quantitative EDX from SnS-SiGt (squares) and SnO₂-SiGt (circles), plotting the content in Sn (a) and the content in O (b) vs the content in Si. As the most abundant element, C is taken as the reference. Lines are best linear fits, slopes are indicated as s values (all fit parameters in Figure S7).

Using the slope and intercept of these correlation curves, and developing a quantitative model taking into account the elemental composition of each phase, we could quantify reliably the O content as presented in Table 2 (refer to supplementary information for complete calculation). It appears first that 10-20% of the oxygen initially present in graphite is eliminated during the growth

process, probably through chemical reduction of C=O or C-OH by the reactive gases, hydrogen or hydrides. As for the SiNW-SnNP component, it contains a significant amount of oxygen when the growth is carried out on SnO₂ seeds, and no detectable oxygen for a growth on SnS seeds. Let us note that, if all the oxygen gathered in a SiO₂ passivation layer on the SiNW surface, the layer would be only 0.7 nm thick (based on the specific area of the material) for SnO₂-SiGt. This very low oxidation, even after months of exposure to air, is possible due to the hydrophobic protection of the SiNW by the native phenyl layer grown from diphenylsilane in our process.¹⁶

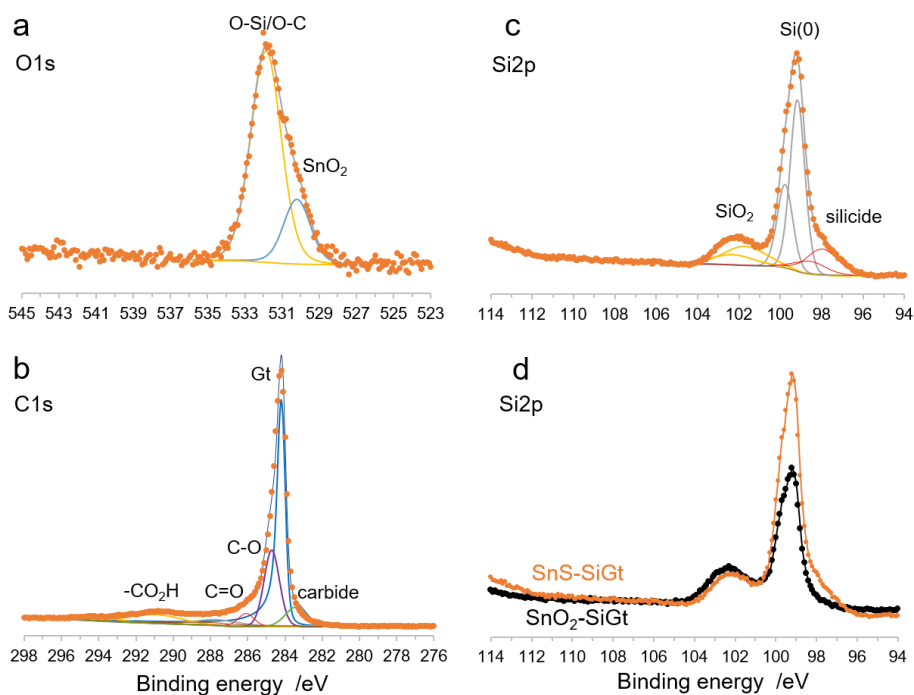


Figure 3. XPS O 1s (a), C 1s (b) and Si 2p (c) spectra of SnS-SiGt. (d) Comparison of SnS-SiGt (orange) and SnO₂-SiGt (black) Si2p spectra. Complete XPS data in Figure S8.

The XPS analysis brings complementary data on the surface composition of the composites. The amount of oxygen of 5 to 6 wt% detected by XPS (Table S1) is much higher than the bulk content measured by EDX, showing that oxygen concentrates at the surface. The O 1s and C 1s spectra are very similar for SnS-SiGt and SnO₂-SiGt (Figure 3 a,b and S8). The C 1s spectra show a main peak at 284.2 eV corresponding to graphite (fitted using a peak model from ref²⁷), and smaller peaks at 287-288 eV due to C-O/C=O/CO₂H species in graphite defects and possible surface contamination. A notable peak at 283.4 eV, attributed to carbides,^{28,29} is due to the Si-C bonds anchoring the native phenyl layer to the SiNW surface, as already reported for SiNWs grown from diphenylsilane.¹⁶ The Sn concentration is lower than measured by EDX because tin is mostly present as large NPs (Figure S4c & S5c), the core of which escapes XPS probing (2-5 nm penetration depth). The Sn signal and the O 1s spectra are consistent with tin in the form of tin oxide SnO₂.

In the Si 2p XPS spectra (Figure 3c), the major signal at 99.2 eV is the Si(0) peak from the SiNW core, indicating that the oxide and phenyl layer present at their surface^{2,16} are very thin. The large peak at 102.5 eV is ascribed to silicon oxides,^{6,30} and the SiO_x/Si(0) ratio is twice larger for SnO₂-SiGt than for SnS-SiGt (Figure 3d), in line with our findings by EDX (Table 1). Finally, a secondary peak at 97 eV appears reproducibly with a significant intensity for SnS-SiGt and to a much lower extent for SnO₂-SiGt. Such peak can only be attributed to silicides that normally appears in metal-silicon alloys.^{31,32} It is not usually observed for Si/Sn systems³³ because the Si concentration in the Si/Sn eutectic is very low,³⁴ so that Si and Sn phase-separate. We attribute this unexpected contribution to a small amount of silicon alloyed in tin, and we assume that Si dissolution in Sn may increase in the presence of S. This may explain why SnS is a more potent catalyst than SnO₂, as we observed from SiNW mass yields.

Electrochemical behavior and cycling performance

Cyclic voltammetry (CV) for SnS-SiGt and SnO₂-SiGt (Figure S9) composite anodes was very similar to our previous findings on Au-seeded SiGt.² A broad cathodic peak at 0.1 V in the first cathodic scan corresponds to crystalline Si alloying with Li and Li intercalation into graphite. Then, the expected anodic peaks at 0.2 V (LiC₆ delithiation), 0.3 and 0.5 V (Li_xSi_y delithiation^{35,36}), and cathodic peaks at 0.2 V (Si lithiation) and 0.06 V (graphite lithiation^{37,38}) were observed. The magnitude of the current peaks increased, suggesting that more material is activated at each scan, until it stabilizes at cycle 5 to 10, ensuring an excellent stability and reversibility. Small peaks characteristic of Sn cycling³³ appear in lithiation at 0.6/0.4 V, and in delithiation at 0.6/0.7/0.8 V, but they only contribute a very low capacity to the anode cycling (the capacity contribution from Sn at 4 wt% translates into only 40 mAh g⁻¹).

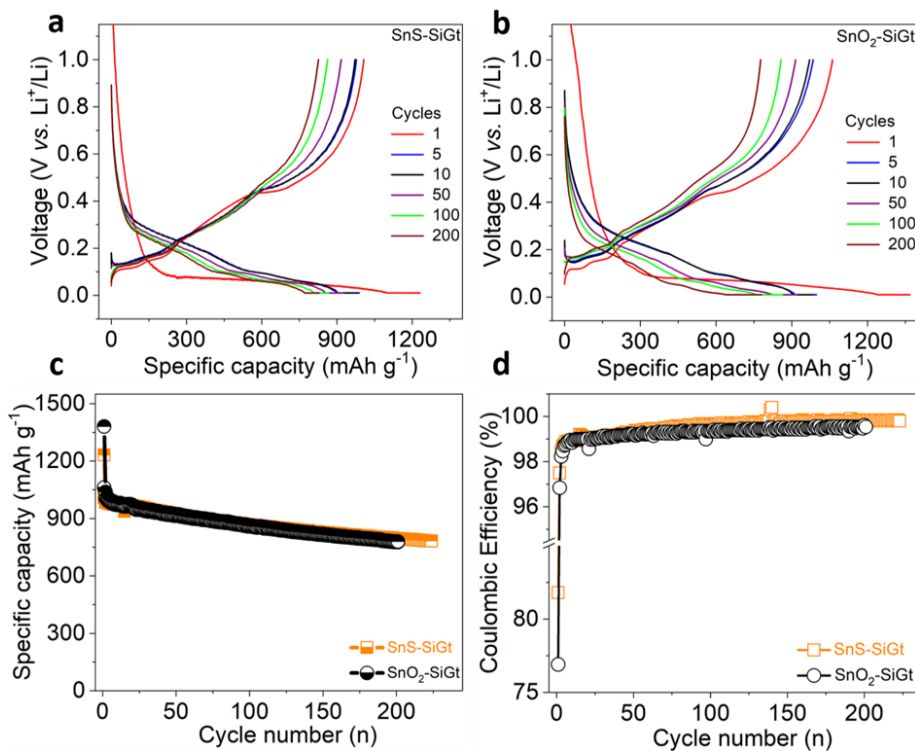


Figure 4. Electrochemical performance of SnS-SiGt and SnO₂-SiGt anodes tested in half-cell configuration vs Li metal. (a,b) Charge-discharge profiles of SnS-SiGt (a) and SnO₂-SiGt (b) cycled at C/5 rate (except cycle 1 at C/20) at room temperature in the 0.01-1.0 V vs Li⁺/Li potential window with 1 M LiPF₆ electrolyte in 1:1 (v/v ethylene carbonate (EC) and diethylene carbonate (DEC) with 2 wt% of vinylencarbonate (VC) and 10 wt% of fluoroethylene carbonate (FEC)). (c, d) Long-term cycling performances of SnS-SiGt (orange squares) and SnO₂-SiGt (black circles) at C/5 rate (1st cycle at C/20): charge/discharge capacity vs cycle number (c), corresponding Coulombic efficiency (d). Mass loading SnS-SiGt 1.7 mg cm⁻², SnO₂-SiGt 1.3 mg cm⁻².

The charge-discharge profiles of SnS-SiGt (Figure 4a) and SnO₂-SiGt (Figure 4b) cycled under galvanostatic-potentiostatic conditions in lithium half cells are found to be similar to those of other SiGt composites from the literature.^{2,39-44} The steady decay of the voltage / capacity profile at the beginning of the first lithiation for both composites relates to the formation of the solid electrolyte interphase (SEI). SnS-SiGt exhibits a lithiation/delithiation capacity of 1230/1000 mAh g⁻¹ during the formation cycle at C/20, with an initial Coulombic efficiency (ICE) of 81%. This ICE is among the highest reported for silicon-rich SiGt composites,^{35,39-45} including our own reports.^{2,15,20} The initial lithiation/delithiation capacity of SnO₂-SiGt is 1370/1060 mAh g⁻¹, with an ICE of 77%. The lower ICE of SnO₂-SiGt compared to that of SnS-SiGt may be associated to the higher surface oxygen content of SnO₂-SiGt.

In the long-term cycling, SnS-SiGt and SnO₂-SiGt exhibit a capacity retention of 82% and 80% (795 and 780 mAh g⁻¹) after 200 cycles from their 10th cycle (Figure 4c), which is better than those of other Si-Gt composites with higher or lower Si content.^{2,35,43,44,46-54} Accordingly, both composites show very similar Coulombic efficiencies in the first 30 cycles (Figure 4d), then the Coulombic efficiency of SnO₂-SiGt stabilizes at 99.5%, while that of SnS-SiGt attains 99.8%. This slight but reproducible difference might ensue from electrochemical loss in SnO₂-SiGt cycling due to a higher oxygen-content in the initial active material and then in the SEI.

Both composites deliver their full theoretical capacity close to 1000 mAh g⁻¹, indicating a full electrochemical utilization of Si and Gt. In other words, our unique advanced material architecture ensures the complete utilization of Si in the anode. A further analysis of the capacity contribution from the potentiostatic phase to the total capacity of SnS/SnO₂-SiGt was performed. The potentiostatic capacity contribution to the total capacity is very low (5-8%, Figure S10), indicating

a high electrode conductivity. This is a hint of maintained mechanical integrity of the electrode throughout cycling.

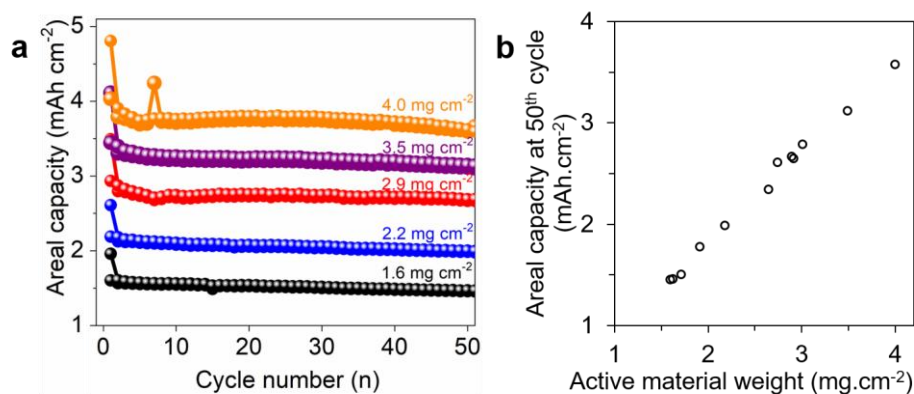


Figure 5. (a) Areal capacity vs cycle number of SnS-SiGt anodes with mass loadings 1.6, 2.2, 2.9, 3.5 and 4.0 mg cm⁻² at C/5 rate in half-cell configuration vs Li metal. Corresponding specific capacity profiles on Figure S11. (b) Areal capacity at 50th cycle vs SnS-SiGt anode loading.

Investigating further on the conductivity of the anode layer, we prepared SnS-SiGt electrodes of increasing thickness with mass loadings ranging from 1.6 to 4.0 mg cm⁻². Figure 5a shows the corresponding areal capacities in cycling. Areal capacities of 1.5, 2.0, 2.7 and 3.2 mAh cm⁻² were attained at mass loadings of 1.6, 2.2, 2.9 and 3.5 mg cm⁻² after 50 cycles at C/5, respectively. This translates in a full linearity of the areal capacity with loading (Figure 5b). Moreover, an areal capacity of 3.6 mAh cm⁻² is obtained even at a high areal mass loading of 4.0 mg cm⁻², qualifying SnS-SiGt among the highest density SiGt electrodes.^{2,3,22-32} The average specific capacity on this series attains the remarkable value of 920 mAh g⁻¹ (Figure S11). In general, because of the poor mechanical stability and low electrical conductivity of silicon-rich electrode, increasing the Si mass loading to achieve the desired areal capacity severely affects the battery performances. Here,

SnS-SiGt demonstrates outstanding stability even at high mass loadings, inferring a complete and effective electrochemical utilization of the whole active material in thick electrodes. This indicates that the SiNW-grown-on-graphite design provides both high Li^+ accessibility and efficient electron transport throughout the whole electrode thickness, a promising asset towards the objective of energy-dense, industrially relevant electrodes delivering up to 5mAh cm^{-2} .

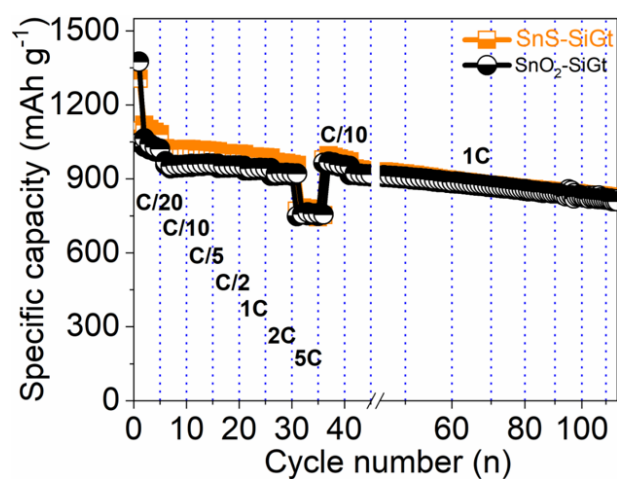


Figure 6. Rate capability behavior of SnS-SiGt (dots) and SnO₂-SiGt (squares) under increasing rates from C/20 to 5C (charge/discharge profiles provided in Figure S13). Mass loading of the electrodes $0.9\text{-}1.0\text{ mg cm}^{-2}$.

Figure 6 displays the rate capability behavior of SiGt anodes. Both composite anodes exhibit a very good rate performance up to the higher current rate of 5C. The observed high capacity of 780 and 760 mAh g^{-1} at 5C rate (for SnS-SiGt and SnO₂-SiGt respectively) is still twice higher than the capacity of commercial graphite cycled at a lower current rate. Moreover, when the current rate is reverted to C/10, a reversible capacity of 990 and 970 mAh g^{-1} (97% capacity retention with respect to the capacity at initial C/10) is recovered readily from SnS-SiGt and SnO₂-SiGt

respectively, further demonstrating the excellent structural and cycling stability. SnS-SiGt and SnO₂-SiGt show a capacity of 840 and 820 mAh g⁻¹ after 100 cycles at 1C with a good capacity retention of 85 and 87% (with respect to 1C) respectively, even after subjecting the cell at higher charge-discharge current rates, demonstrating excellent rate performance. Moreover, the potentiostatic capacity contribution still stays well within the acceptable limit, below 15% up to 2C, and only 22-23% at 5C (Figure S13c). It endorses the high electronic conductivity of the electrode *via* efficient interconnection between SiNWs and Gt.

Therefore, our results indicate that the choice of SnS or SnO₂ as the SiNW seeds has no or very little effect on the rate capability of the SiGt anode. Instead, the SiGt rate capability is mainly sensitive to the electrode mass loading (Figure S12). As the electrical conductivity of the SiGt electrode proved very high from low potentiostatic capacity, this hints towards a main limitation in lithium ion diffusion along the electrode thickness at very high current density.

Post-mortem morphology characterization: pristine vs cycled electrodes

In order to achieve a better understanding of the good electrochemical results of SiGt, we ran pristine and post-mortem focused-ion beam sampling-scanning electron microscopy (FIB-SEM) analysis on the SnS-SiGt samples (Figure 7). Similarly to our first study on gold-seeded SiGt,² part of the SiNWs were embedded inside the graphite particles, between the flakes as clearly seen in Figures 7a and b. As shown on the FIB-SEM images, the as-synthesized composite contains finely mixed SiNWs and graphite whose contact zones are wide and multiple, thus promoting the electron and Li⁺ exchanges between the two phases. SnS-SiGt can be described as micro-sized particles of SiNWs embedded in graphite. In fact, the main porosity in the electrode comes from the space between the SiGt particles, that could be reduced by varying the graphite size.⁵⁵

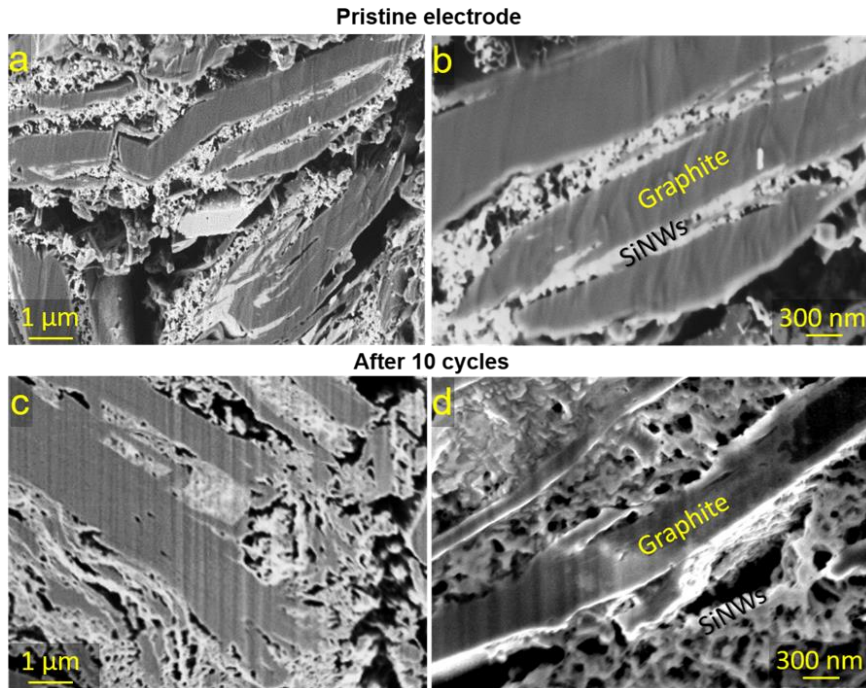


Figure 7. Morphological evolution upon cycling by cross-sectional FIB-SEM of SnS-SiGt electrodes: in pristine state (a) and after 10 cycles (b).

In the close-up image on Figure 7b, additional nanoporosity is clearly seen. This internal nanoporosity provides enough space for silicon swelling and electrolyte access, beneficial for cycling without adding over-proportionated porosity. Figure 7c and d show FIB-SEM images of the SnS-SiGt electrode after 10 cycles, in the lithiated state. The intimate mix between SiNWs and graphite remains the same, and nanoporosity is still present to let the electrolyte penetrate the sample, thus providing good rate performances by allowing fast exchanges with both phases.

Summarizing, the overall improved electrochemical performances of SiGt composite anodes using Sn based catalysts presented in this work could be ascribed to the following aspects:

(i) The specifically designed architecture provides the key features required to obtain stable electrochemical performances in terms of capacity, stability, and rate capability with the industrially accepted active material loading, such as uniform distribution of SiNWs and the effective ratio between Si and graphite.

(ii) The growth process provides an effective connection between graphite and silicon, mechanically resilient and electrically stable. Besides, the nanoporosity in between the SiNWs insures good, durable contact with the electrolyte. All active materials thus fully participate in the electrochemical reactions even at very high loading *via* offering high overall electrode conductivity throughout cycling and the formation of a stable SEI layer.

(iii) With the addition of commercially well proven graphite anode, mechanical integrity of the composite electrode is highly preserved throughout cycling by effective accommodation of the Si volume changes.²

CONCLUSION

Looking for a lower-cost and more sustainable synthesis of high-energy-density silicon-graphite composites, we show that replacing Au catalysts by Sn-based nanoparticles induces an increased capacity, long-term cycling stability and high initial Coulombic efficiency at an industrial electrode density of 1.6 g cm^{-3} . It also allows the reduction of the synthesis temperature by 50°C , and thus a drop-in energy consumption. SnS is more efficient than SnO_2 as seeds for SiNW growth on graphite, but both produce SiGt composites with similar structural characteristics. A difference appears, however, in the elemental composition of the composites. The small gap in composition between SnS- and SnO_2 -seeded composites could be reliably evidenced by developing an accurate analysis method based on the widely available EDX analytical tool. The oxygen contained in the

SnO₂ seeds ends up in the SnO₂-SiGt composite as a thin SiO₂ layer that induces a lower initial Coulombic efficiency, and possibly a slight long-term drop in Coulombic efficiency. As for the SnS seeds, very little sulfur finally enters in the SnS-SiGt composite, but an unexpected effect of SnS seeding is an increased dissolution of Si in the eutectic droplets. This feature is currently under study, as it favors a faster growth process, and thus an additional cost reduction. Our proof-of-concept offers insights into the rational design of low-cost high-energy silicon-graphite composites with high Si loading for advanced electrochemical energy storage.

EXPERIMENTAL METHODS

Materials. Thioacetamide, oleylamine, trioctylphosphine, carboxymethylcellulose sodium (CMC), tin (IV) oxide (SnO₂), tin (II) chloride (SnCl₂) and sodium chloride NaCl were purchased from Sigma Aldrich. Diphenylsilane was purchased from ChemicalPoint, Germany. Graphite (grade: SLP-30 and specific surface area: 6.5 m²/g) and carbon black Super-P (CB) were purchased from TIMCAL.

SnS NCs synthesis. SnS NCs of 6 nm diameter (Figure S1) were synthesized as previously described.⁵⁶ Solution A, a solution of SnCl₂ (380 mg, 2 mmol), ocatadecene (5 mL, 15.6 mmol), trioctylphosphine (3 mL, 6.7mmol) and oleic acid (4,5 mL, 14.3 mmol) is degassed under vacuum at 60 °C for 1 h. Solution A is then heated to 120°C under Argon. Solution B, a solution of thioacetamide (75 mg, 1 mmol), trioctylphosphine (3 mL, 6.7 mmol), oleylamine (5 mL, 15.2 mmol) is quickly added to solution A with a syringe under fast stirring. After 5 minutes of reaction, the medium is cooled down with an ice bath. Chloroform (20 mL) and ethanol (40 mL) are added and the suspension is centrifuged (5000 rpm, 3 minutes). The supernatant is removed and the nanoparticles are mixed again with 10 mL chloroform and 20 mL ethanol. After centrifugation (5000 rpm, 3 minutes) the transparent supernatant is removed. The agglomerated SnS NCs are

finally dispersed in 10 mL chloroform. The concentration of SnS NCs is determined by drying a 100 μ L drop of the colloidal solution and adjusted to 13 mg/mL.

SiNW growth on graphite. SiNWs are grown in a stainless-steel pressure reactor of inner volume 150 cm³ heated by induction, as described previously.^{2,15} SnS NCs (80 mg) in chloroform diluted in 5 mL of hexane/isooctane 10:1 or SnO₂ NPs (\leq 50 nm, 80 mg) in water diluted in 5 mL of ethanol is added to 800 mg of graphite (SLP30) in a warm mortar (80 °C). The mixture is ground with a pestle until complete evaporation of the solvent. The SnS NCs or SnO₂ NPs-loaded graphite is sealed with diphenylsilane (12 mL) in the reactor under vacuum before heating at 390 °C for 5 h. After cooling down, the collected black powder is washed thrice with dichloromethane to remove impurities and dried at 80 °C to yield SnS-SiGt or SnO₂-SiGt (1120 mg, roughly 22-23 wt% of Si), respectively. Growth of reference pure SiNWs was done as previously reported^{15,16} by using finely ground NaCl powder as a sacrificial substrate loaded with SnS NCs or SnO₂ NPs as described above. NaCl was removed by washing with water after growth. At least 8 batches were grown for each material (SnS-SiGt, SnO₂-SiGt, SnS-seeded SiNWs).

Materials characterization. Phase characterization was performed with powder X-ray diffraction technique on a Bruker D8 advance diffractometer θ -2 θ configuration with a Cu anode. We used a scanning step of 0.02° and a counting time of 1.2 s per step. Scanning Electron microscopy was operated on a Zeiss Ultra 55 microscope at an accelerating voltage of 5 kV and a working distance of 5 mm. For TEM and HRTEM observations, a JEOL 2010 high resolution transmission electron microscope (HRTEM) operated at 200 kV was used. For TEM measurements, the powder was dispersed in ethanol and nanoparticles separated with intensive ultrasound using the Hielscher Ultrasound Technology VialTweeter UIS250V. Then, the dispersion was dropped on a grid made of a Lacey Carbon Film (300 mesh Copper – S166-3H).

X-ray photoelectron spectroscopy (XPS) analyses were carried out with a Versa Probe II spectrometer (ULVAC-PHI) equipped with a monochromated Al K α source ($h\nu = 1486.6$ eV). The core-level peaks were recorded with a constant pass energy of 23.3 eV. The XPS spectra were fitted with CasaXPS 2.3 software using Shirley background. Binding energies (BEs) are referenced with respect to adventitious carbon (C 1s BE = 284.8 eV). The Brunauer, Emmet, and Teller (BET) method was used to measure the SBET specific surface of the different samples using a Micromeritic apparatus (Tristar II and Flowsorb 2300).

Electrochemical characterization. The electrode was fabricated from a mixture containing active material, super P carbon black (additive) and CMC (binder) diluted in pure distilled water in the weight ratio of 80:10:10. The resultant slurry was coated using doctor blade method on thin copper foil (12 μm) and dried at 80 $^{\circ}\text{C}$ for overnight (mass loading 1.6-1.7 mg cm^{-2} unless otherwise stated, thickness 20 μm). The Celgard separator was soaked with an electrolyte of 1 M LiPF $_6$ in 1:1 v/v ethylene carbonate (EC) and diethylene carbonate (DEC) with 2 wt% of vinylencarbonate and 10 wt% of fluoroethylene carbonate. 2032 coin cells were assembled with lithium metal as reference and counter electrode in an Argon-filled glove box and crimp sealed. Electrochemical properties of the half-cells were evaluated in the potential window between 0.01 V to 1.0 V. Along the manuscripts all the potentials measured in half cell configuration refer to Li metal counter electrode and are thus expressed as *vs* Li $^{+}$ /Li. All the capacity values shown in this paper are based on the total mass of the active material, unless otherwise stated (theoretical capacities and electrochemical test details in Tables S2 and S3). Electrochemical studies, including electrochemical impedance spectroscopy, were carried out using Biologic VMP3 multichannel potentiostat and ARBIN charge–discharge cycle life tester. At least 50 cells prepared from at least 8 different batches were tested for each composite SnS-SiGt and SnO $_2$ -SiGt. Direct comparison

were obtained from at least two independent material and electrode sets on simultaneous electrochemical tests in triplicate.

Quantitative Energy Dispersive X-ray Spectroscopy. 2 mg of composite were pressed into a 5 mm-diameter pellet in a hydraulic press (Specac) under 2 tons of pressure for 2 minutes, to obtain a dense sample (>85%) with a flat surface, to allow for a quantitative analysis. Energy Dispersive X-ray spectroscopy (EDX) spectra were recorded on a Zeiss Ultra 55+ microscope at an accelerating voltage of 10 kV at working distance of 7 mm. The apparatus was first calibrated with a series of elemental standards (Zeiss). A dozen scans were then recorded on each pellet, first on wide zones (typically 500x500 μm^2) to determine the average composition, then on small zones (typically 20x20 μm^2) for correlations.

FIB-SEM imaging. The disassembled electrodes were transferred through a special transfer holder from the glove box to a Zeiss NVision 40 focused ion beam (FIB-SEM) without air exposure. SEM images were acquired using secondary electron (SE) and energy selective backscattered electron (BSE) detectors with a primary beam energy of 2 kV. Current is not monitored on the NVision microscope but an aperture of 60 μm was used to acquire all images at a roughly constant 2 nA current. Details of the sample preparation steps are given in ref⁶⁷. Coarse trenches were dug at 30 kV, 15 nA. The cross section polishing and cleaning was carried out at 30 kV and a low beam current of 690 pA. Considering the smaller size of SiNWs (typically 40 nm), global SEM images were recorded with a pixel size of 30 nm and the close-ups were recorded at a pixel size of 5 nm.

ASSOCIATED CONTENT

Supporting Information. The Supporting Information is available free of charge on the ACS Publications website. Figures S1-S13 and Tables S1-S3 as described in the text, specifically,

additional SEM, STEM, XRD, XPS, correlation diagram for EDX analysis, pressure-temperature recording for the synthesis, electrochemical performances, and comparison parameters with the recent literature reports.

AUTHOR INFORMATION

Corresponding Authors

E-mail: pascale.chenevier@cea.fr

E-mail: cedric.haon@cea.fr

Code de champ modifié

Author Contributions

S.K and C.K contributed equally to this work. S.K. and M.R. prepared the materials, electrodes and performed the electrochemical tests. C.K. and P.R. made the AuNPs and SnS NCs. C.K. prepared part of the composites and performed chemical characterization. P.C., J.W. and S.K. performed SEM and TEM analysis. D.A. performed the XPS analysis. M.R. and P.C. performed the EDX correlation analysis. S.K., P.C., C.K. and C.H. conceived and designed the experiments and wrote the manuscript. P.R., P.C. and C.H. insured supervision and funding. All authors discussed the results and commented on the manuscript.

Funding Sources

“The authors declare no competing financial interest.”

ACKNOWLEDGMENT

S.K. acknowledges the financial support from European Project Flagship Graphene Core 2 under grant agreement no. 785219. J.W. acknowledges the financial support from European Horizon

2020's Project Sun-to-X under agreement no. 883264. The authors thank Daniel Tomasi for helping in electrode preparation and Agnès Brun for BET analysis.

REFERENCES

- 1 C.-H. Yim, S. Niketic, N. Salem, O. Naboka and Y. Abu-Lebdeh, *J. Electrochem. Soc.*, 2016, **164**, A6294.
- 2 S. Karuppiyah, C. Keller, P. Kumar, P.-H. Jouneau, D. Aldakov, J.-B. Ducros, G. Lapertot, P. Chenevier and C. Haon, *ACS Nano*, 2020, **14**, 12006–12015.
- 3 V. Schmidt, J. V. Wittemann and U. Gösele, *Chem Rev*, 2010, **110**, 361–388.
- 4 A. M. Chockla, T. D. Bogart, C. M. Hessel, K. C. Klavetter, C. B. Mullins and B. A. Korgel, *The Journal of Physical Chemistry C*, 2012, **116**, 18079–18086.
- 5 US 10,243,207 B2, .
- 6 B. Liu, P. Huang, Z. Xie and Q. Huang, *Energy Fuels*, , DOI:10.1021/acs.energyfuels.0c03725.
- 7 S. Imtiaz, I. S. Amiin, D. Storan, N. Kapuria, H. Geaney, T. Kennedy and K. M. Ryan, *Advanced Materials*, 2021, **n/a**, 2105917.
- 8 A. M. Chockla, K. C. Klavetter, C. B. Mullins and B. A. Korgel, *Chemistry of Materials*, 2012, **24**, 3738–3745.
- 9 E. Sutter, F. Ivars-Barcelo and P. Sutter, *Particle & Particle Systems Characterization*, 2014, **31**, 879–885.
- 10 H. F. Al-Taay, M. A. Mahdi, D. Parlevliet and P. Jennings, *Materials Science in Semiconductor Processing*, 2013, **16**, 15–22.
- 11 A. de Kergommeaux, M. Lopez-Haro, S. Pouget, J. M. Zuo, C. Lebrun, F. Chandezon, D. Aldakov and P. Reiss, *Journal of the American Chemical Society*, 2015, **137**, 9943–9952.
- 12 H. Song, H. X. Wang, Z. Lin, L. Yu, X. Jiang, Z. Yu, J. Xu, L. Pan, M. Zheng, Y. Shi and K. Chen, *Nano Energy*, 2016, **19**, 511–521.
- 13 L. Dai, I. Maurin, M. Foldyna, J. Alvarez, W. Wang, H. Mohsin, W. Chen, J.-P. Kleider, J.-L. Maurice, T. Gacoin and P. R. i Cabarrocas, *Nanotechnology*, 2018, **29**, 435301.
- 14 E. Mullane, T. Kennedy, H. Geaney, C. Dickinson and K. M. Ryan, *Chemistry of Materials*, 2013, **25**, 1816–1822.
- 15 C. Keller, A. Desrués, S. Karuppiyah, E. Martin, J. P. Alper, F. Boismain, C. Villevieille, N. Herlin-Boime, C. Haon and P. Chenevier, *Nanomaterials*, 2021, **11**, 307.
- 16 O. Burchak, C. Keller, G. Lapertot, M. Salaün, J. Danet, Y. Chen, N. Bendiab, B. Pépin-Donat, C. Lombard, J. Faure-Vincent, A. Vignon, D. Aradilla, P. Reiss and P. Chenevier, *Nanoscale*, 2019, **11**, 22504–22514.
- 17 D. C. Lee, T. Hanrath and B. A. Korgel, *Angew Chem Int Ed Engl*, 2005, **44**, 3573–7.
- 18 G. Flynn, K. Stokes and K. M. Ryan, *Chem. Commun.*, 2018, **54**, 5728–5731.
- 19 X. Lu, K. J. Anderson, P. Boudjouk and B. A. Korgel, *Chemistry of Materials*, 2015, **27**, 6053–6058.
- 20 C. Keller, Y. Djeddar, J. Wang, S. Karuppiyah, G. Lapertot, C. Haon and P. Chenevier, *Nanomaterials*, 2022, **12**, 2601.
- 21 J. A. Toledo-Antonio, R. Gutiérrez-Baez, P. J. Sebastian and A. Vázquez, *Journal of Solid State Chemistry*, 2003, **174**, 241–248.
- 22 S. A. Zaki, M. I. Abd-Elrahman, A. A. Abu-Sehly, M. Almokhtar, A. S. Soltan and N. M. Shaalan, *Solar Energy*, 2021, **228**, 206–215.

- 23 D. Wang, P. Garra, F. Szillat, J. P. Fouassier and J. Lalevée, *Macromolecules*, 2019, **52**, 3351–3358.
- 24 M. Jeon, J. Han and J. Park, *ACS Catalysis*, 2012, **2**, 1539–1549.
- 25 M. Y. Bashouti, K. Sardashti, J. Ristein and S. Christiansen, *Nanoscale Research Letters*, 2013, **8**, 41.
- 26 J. Shin, T.-H. Kim, Y. Lee and E. Cho, *Energy Storage Materials*, 2020, **25**, 764–781.
- 27 T. R. Gengenbach, G. H. Major, M. R. Linford and C. D. Easton, *Journal of Vacuum Science & Technology A*, 2021, **39**, 013204.
- 28 S. P. Pujari, A. D. Filippov, S. Gangarapu and H. Zuilhof, *Langmuir*, 2017, **33**, 14599–14607.
- 29 M. Y. Bashouti, C. A. Garzuzi, M. de la Mata, J. Arbiol, J. Ristein, H. Haick and S. Christiansen, *Langmuir*, 2015, **31**, 2430–2437.
- 30 S. Jiang, B. Hu, R. Sahore, L. Zhang, H. Liu, L. Zhang, W. Lu, B. Zhao and Z. Zhang, *ACS Appl. Mater. Interfaces*, 2018, **10**, 44924–44931.
- 31 R. Würz, M. Schmidt, A. Schöpke and W. Fuhs, *Applied Surface Science*, 2002, **190**, 437–440.
- 32 W. Liu, J. Liang, X. Zhou and X. Long, *Materials Letters*, 2014, **122**, 220–222.
- 33 B. Ma, J. Luo, X. Deng, Z. Wu, Z. Luo, X. Wang and Y. Wang, *ACS Appl. Nano Mater.*, 2018, **1**, 6989–6999.
- 34 M. J. Loveridge, R. Malik, S. Paul, K. N. Manjunatha, S. Gallanti, C. Tan, M. Lain, A. J. Roberts and R. Bhagat, *RSC Adv.*, 2018, **8**, 16726–16737.
- 35 S. Zhu, J. Zhou, Y. Guan, W. Cai, Y. Zhao, Y. Zhu, L. Zhu, Y. Zhu and Y. Qian, *Small*, 2018, **14**, 1802457.
- 36 W. An, B. Gao, S. Mei, B. Xiang, J. Fu, L. Wang, Q. Zhang, P. K. Chu and K. Huo, *Nat Commun*, 2019, **10**, 1447.
- 37 C. K. Chan, H. Peng, G. Liu, K. Mellwrath, X. F. Zhang, R. A. Huggins and Y. Cui, *Nature Nanotechnology*, 2008, **3**, 31–35.
- 38 X. Li, M. Gu, S. Hu, R. Kennard, P. Yan, X. Chen, C. Wang, M. J. Sailor, J.-G. Zhang and J. Liu, *Nat Commun*, 2014, **5**, 4105.
- 39 S.-H. Choi, G. Nam, S. Chae, D. Kim, N. Kim, W. S. Kim, J. Ma, J. Sung, S. M. Han, M. Ko, H.-W. Lee and J. Cho, *Adv. Energy Mater.*, 2019, **9**, 1803121.
- 40 S. Jeong, J.-P. Lee, M. Ko, G. Kim, S. Park and J. Cho, *Nano Lett.*, 2013, **13**, 3403–3407.
- 41 S. Chae, S.-H. Choi, N. Kim, J. Sung and J. Cho, *Angew. Chem. Int. Ed.*, 2020, **59**, 110–135.
- 42 D. Lin, Z. Lu, P.-C. Hsu, H. R. Lee, N. Liu, J. Zhao, H. Wang, C. Liu and Y. Cui, *Energy Environ. Sci.*, 2015, **8**, 2371–2376.
- 43 M. Ko, S. Chae, J. Ma, N. Kim, H.-W. Lee, Y. Cui and J. Cho, *Nat Energy*, 2016, **1**, 16113.
- 44 X. Li, P. Yan, X. Xiao, J. H. Woo, C. Wang, J. Liu and J.-G. Zhang, *Energy Environ. Sci.*, 2017, **10**, 1427–1434.
- 45 M. N. Obrovac and V. L. Chevrier, *Chem. Rev.*, 2014, **114**, 11444–11502.
- 46 S. Chae, M. Ko, S. Park, N. Kim, J. Ma and J. Cho, *Energy Environ. Sci.*, 2016, **9**, 1251–1257.
- 47 S. Jiang, B. Hu, Z. Shi, W. Chen, Z. Zhang and L. Zhang, *Advanced Functional Materials*, 2020, **30**, 1908558.
- 48 N. Kim, S. Chae, J. Ma, M. Ko and J. Cho, *Nat Commun*, 2017, **8**, 812.
- 49 S. Y. Kim, J. Lee, B.-H. Kim, Y.-J. Kim, K. S. Yang and M.-S. Park, *ACS Appl. Mater. Interfaces*, 2016, **8**, 12109–12117.
- 50 Q. Xu, J.-Y. Li, J.-K. Sun, Y.-X. Yin, L.-J. Wan and Y.-G. Guo, *Adv. Energy Mater.*, 2017, **7**, 1601481.

- 51 H. Su, A. A. Barragan, L. Geng, D. Long, L. Ling, K. N. Bozhilov, L. Mangolini and J. Guo, *Angewandte Chemie International Edition*, 2017, **56**, 10780–10785.
- 52 S. Kim, Y. K. Jeong, Y. Wang, H. Lee and J. W. Choi, *Adv. Mater.*, 2018, **30**, 1707594.
- 53 M. H. Parekh, A. D. Sediako, A. Naseri, M. J. Thomson and V. G. Pol, *Advanced Energy Materials*, 2020, **10**, 1902799.
- 54 P. Li, J.-Y. Hwang and Y.-K. Sun, *ACS Nano*, 2019, **13**, 2624–2633.
- 55 J. Hou, M. Yang, L. Zhou, X. Yan, C. Ke and J. Zhang, *Advanced Materials Technologies*, 2021, **6**, 2100152.
- 56 A. de Kergommeaux, J. Faure-Vincent, A. Pron, R. de Bettignies, B. Malaman and P. Reiss, *Journal of the American Chemical Society*, 2012, **134**, 11659–66.
- 57 P. Kumar, C. L. Berhaut, D. Z. Dominguez, E. D. Vito, S. Tardif, S. Pouget, S. Lyonard and P.-H. Jouneau, *Small*, 2020, **16**, 1906812.